Selective optimisation of catalytic activity by tuning the structural composition in nanoparticulate $CuFe_2O_4$

-

J. Zander, M. F. Fink, M. Attia, C. Roth, R. Marschall

-

Supporting Information

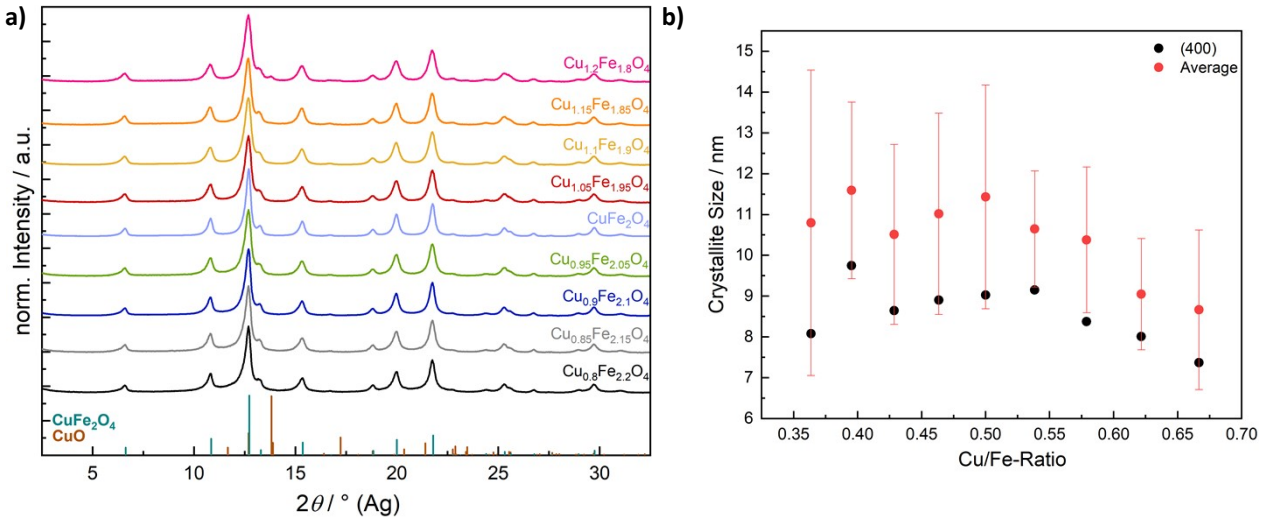

Figure S1 Ag-XRD patterns for $CuFe_2O_4$ with different Cu/Fe-ratios elucidating phase-purity over a wide range of compositions (a) and crystallite sizes determined by the integral breadth method from the Cu-XRD data (b).

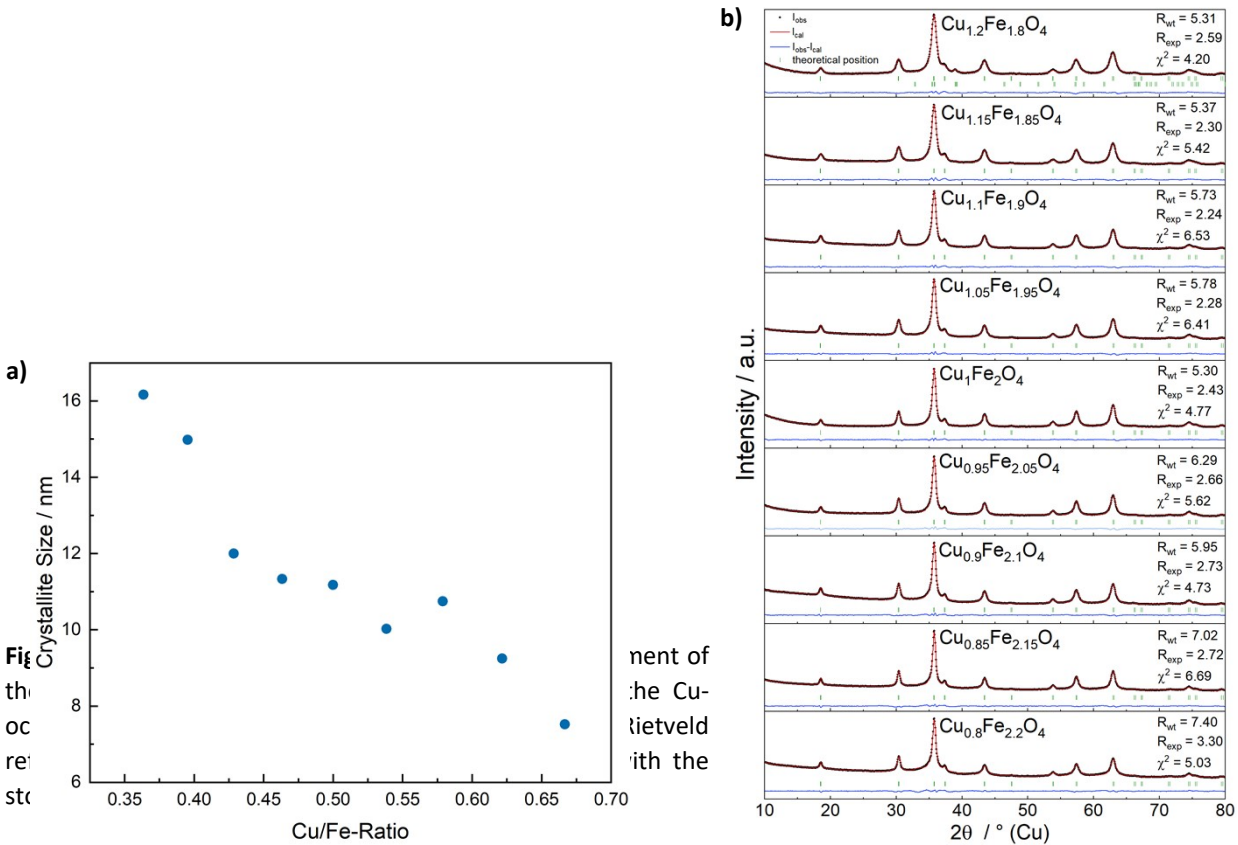

Fig nent of
th he Cu-
oc ietveld
re ith the
st

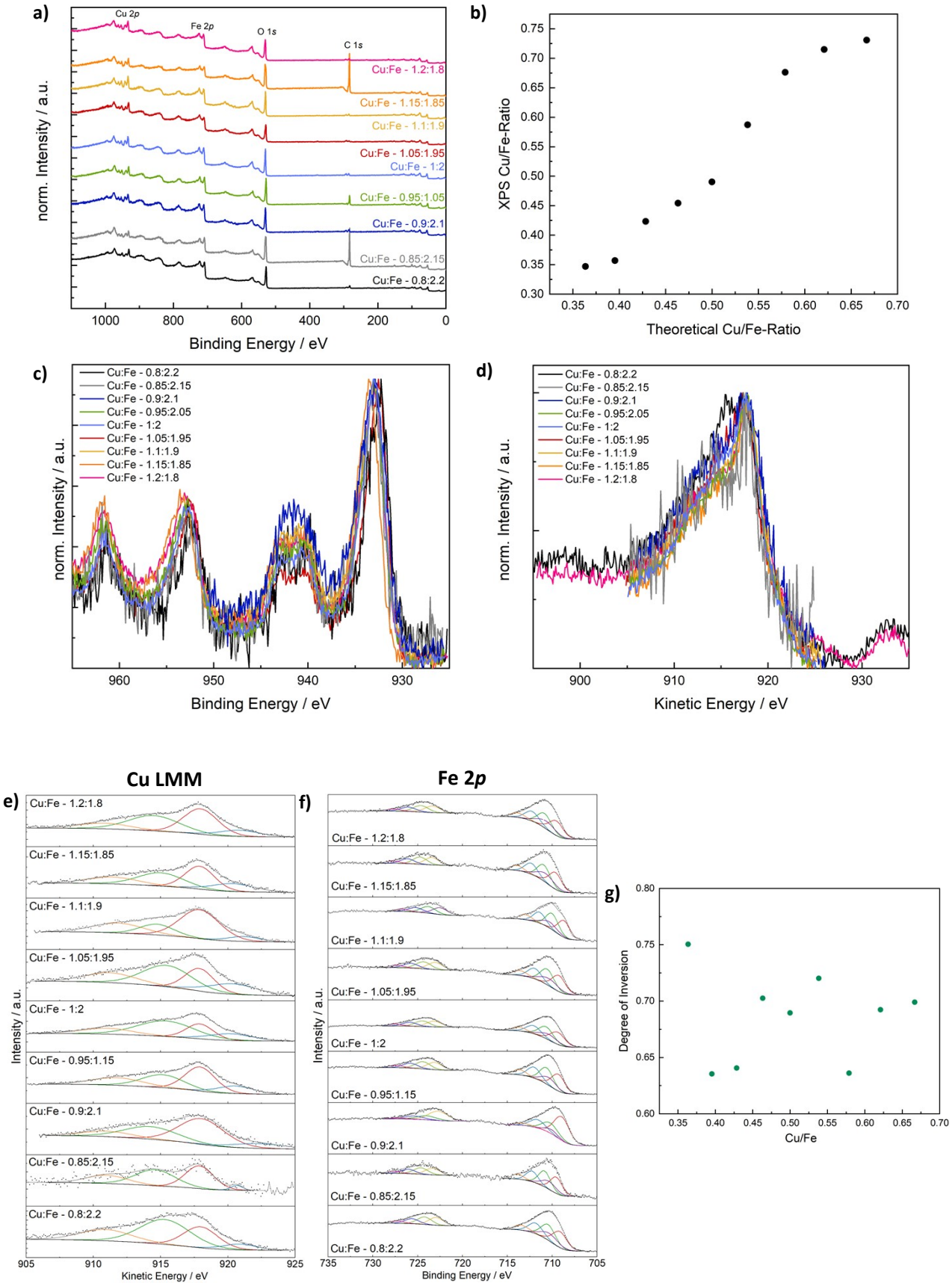

Figure S3 XP spectra of $CuFe_2O_4$ with different Cu/Fe-ratios. Survey scans are shown in (a), derived Cu/Fe ratios in (b), normalised Cu 2*p* spectra in (c), normalised Cu $L_3M_{4,5}M_{4,5}$ Auger spectra in (d) and the derived degree of inversion in (g). The fitted Cu $L_3M_{4,5}M_{4,5}$ spectra and Fe 2*p* spectra are shown in (e) and (f), respectively. The parameters for CuO (Auger) and $NiFe_2O_4$ (Fe 2*p*) reported by Biesinger *et al.* were used for the fit.[1,2]

Table S1 Elemental composition derived from XPS survey scans.

Cu:Fe- Ratio	Cu / at.%	Fe / at.%	O / at.%	C / at.%	K / at.%	Si / at.%	Cu/Fe
0.8:2.2	7.42	21.39	54.7	14.78	1.38	0.33	0.35
0.85:2.15	2.61	7.31	29.18	58.96		1.68	0.36
0.9:2.1	10.02	23.67	49.45	11.42	1.4	4.03	0.42
0.95:2.05	7.38	16.25	44.17	30.34	0.47	1.39	0.45
1:2	10.44	21.29	55.08	8.06	1.42	3.71	0.49
1.05:1.95	11.13	18.96	57.28	7.1	2.17	3.37	0.59
1.1:1.9	13.04	19.29	54.63	7.9	1.33	3.8	0.68
1.15:1.855	3.41	4.77	26.69	63.21		1.93	0.71
1.2:1.8	12.76	17.46	59.3	6.77	0.85	2.86	0.73

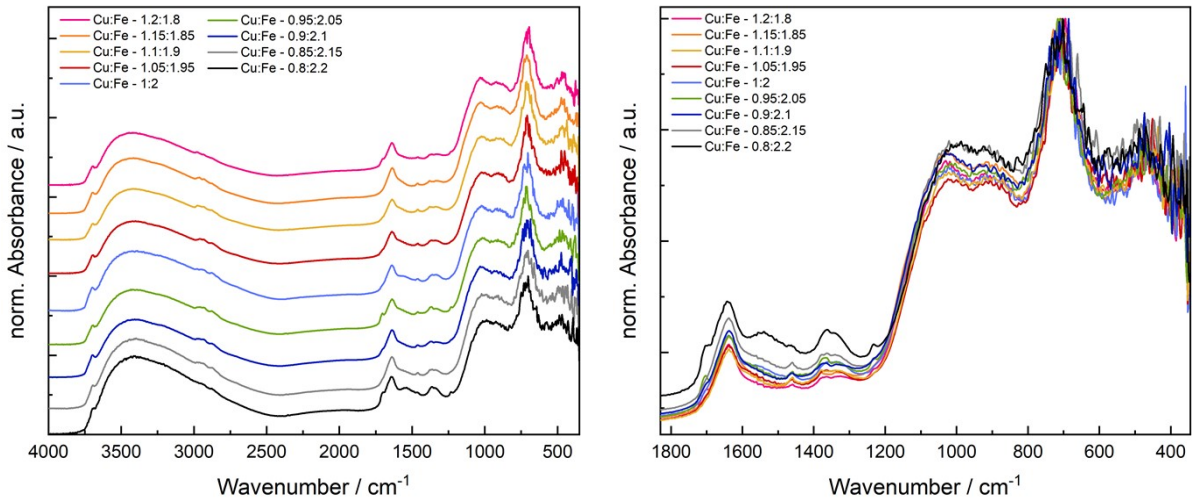

Figure S4 DRIFT spectra of $CuFe_2O_4$ with different Cu/Fe-ratios, showing a similar amount of residual surface organics from the synthesis and highly comparable relative intensities for M-O vibrations at tetrahedral and octahedral sites, suggesting strong structural similarities.

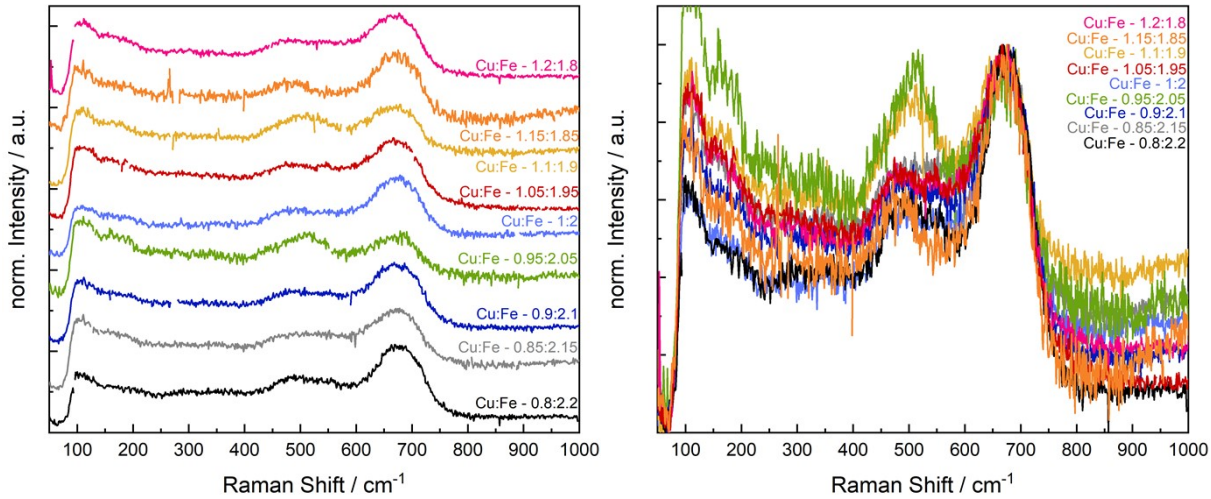

Figure S5 Raman spectra of $CuFe_2O_4$ with different Cu/Fe-ratios, elucidating the absence of Fe-oxide impurities and supporting structural comparability.

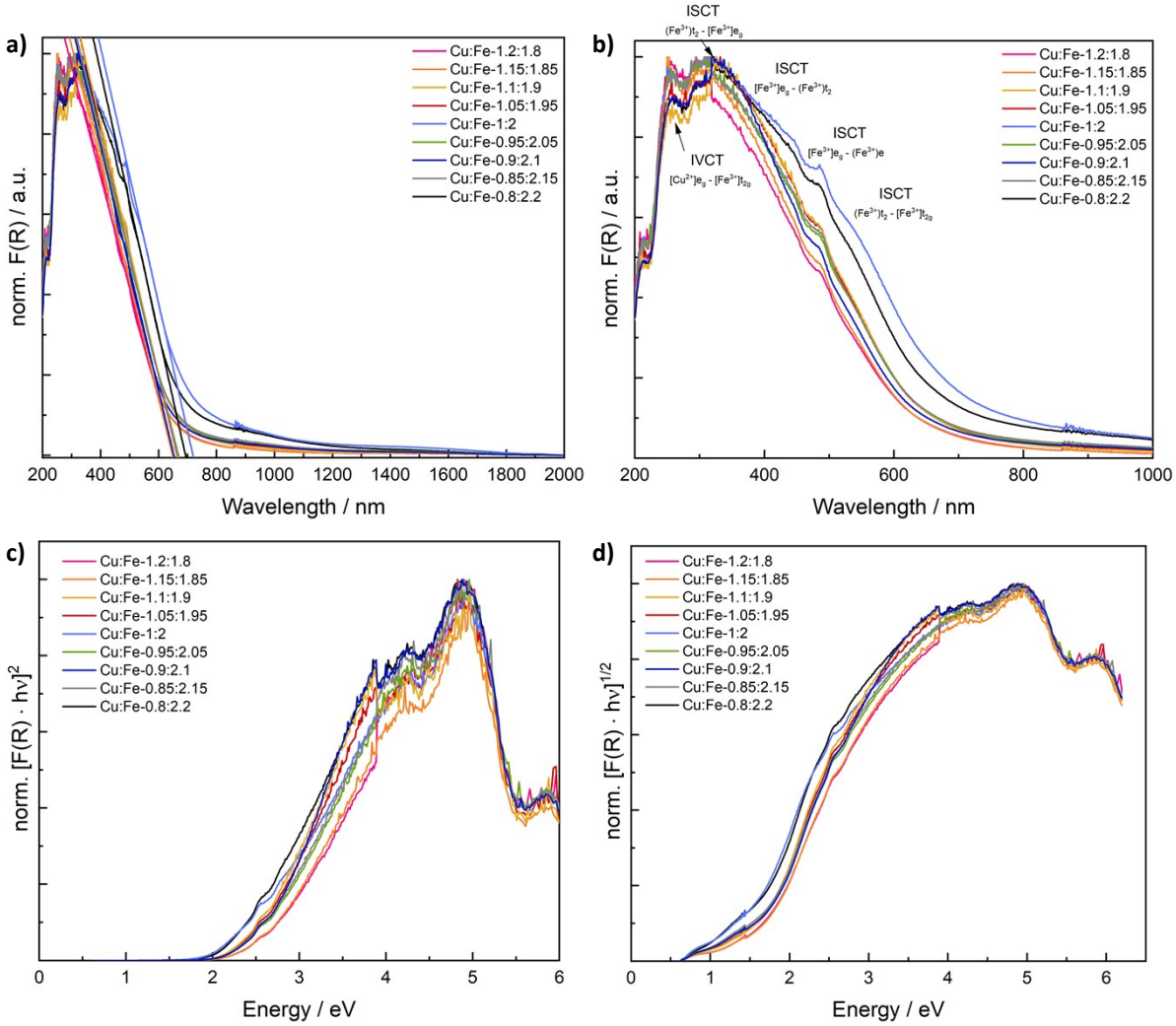

Figure S6 UV/vis measurements of $CuFe_2O_4$ with different Cu/Fe-ratios. Fitted Kubelka-Munk plots are shown in (a), optical charge transfer transitions are elucidated in (b) and direct and indirect Tauc plots are depicted in (c) and (d), respectively.

Table S2 Band gap values of $CuFe_2O_4$ with different Cu/Fe-ratios.

Cu:Fe- Ratio	Kubelka-Munk	direct Tauc	indirect Tauc
0.8:2.2	693 nm/ 1.79 eV	2.33 eV	1.47 eV/ 0.75 eV
0.85:2.15	667 nm/ 1.86 eV	2.49 eV	1.53 eV/ 0.74 eV
0.9:2.1	653 nm/ 1.90 eV	2.59 eV	1.59 eV/ 0.76 eV
0.95:2.05	669 nm/ 1.85 eV	2.51 eV	1.54 eV/ 0.75 eV
1:2	719 nm/ 1.72 eV	2.31 eV	1.42 eV/ 0.78 eV
1.05:1.95	664 nm/ 1.87 eV	2.49 eV	1.55 eV/ 0.81 eV
1.1:1.9	665 nm/ 1.86 eV	2.49 eV	1.56 eV/ 0.82 eV
1.15:1.855	649 nm/ 1.91 eV	2.56 eV	1.57 eV/ 0.86 eV
1.2:1.8	651 nm/ 1.90 eV	2.56 eV	1.55 eV/ 0.88 eV

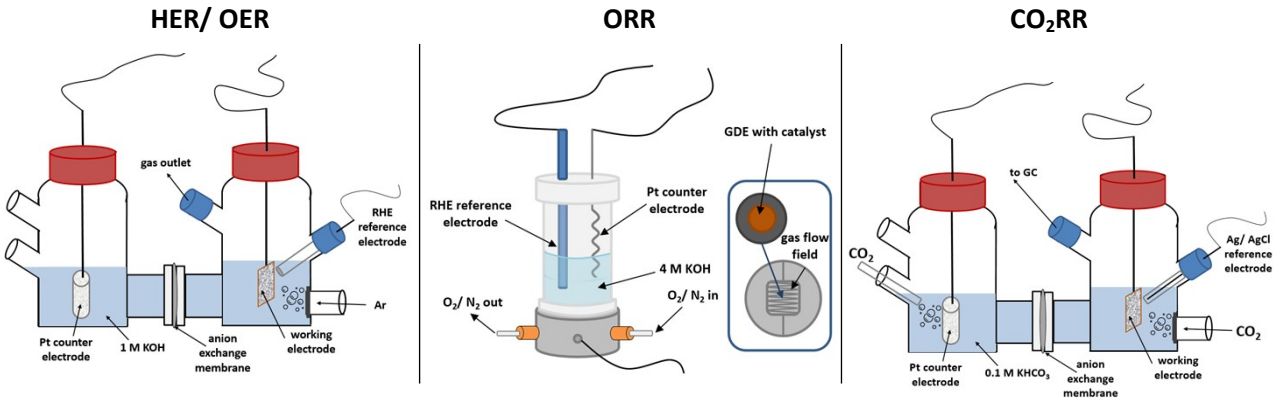

Figure S7 Schemes of reaction cells/ setups employed in this study.

Table S3 Overpotentials for the HER and OER with $CuFe_2O_4$ with different Cu/Fe-ratios.

Cu:Fe- Ratio	η_{HER} – 10 mAcm^{-2}	η_{HER} – 100 mAcm^{-2}	η_{OER} – 10 mAcm^{-2}	η_{OER} – 5 mAcm^{-2}
0.8:2.2	415 mV	577 mV	--	721 mV
0.85:2.15	401 mV	574 mV	--	708 mV
0.9:2.1	433 mV	579 mV	--	697 mV
0.95:2.05	405 mV	516 mV	735 mV	671 mV
1:2	394 mV	559 mV	--	749 mV
1.05:1.95	374 mV	499 mV	765 mV	665 mV
1.1:1.9	357 mV	485 mV	764 mV	674 mV
1.15:1.855	371 mV	507 mV	684 mV	589 mV
1.2:1.8	342 mV	488 mV	--	690 mV

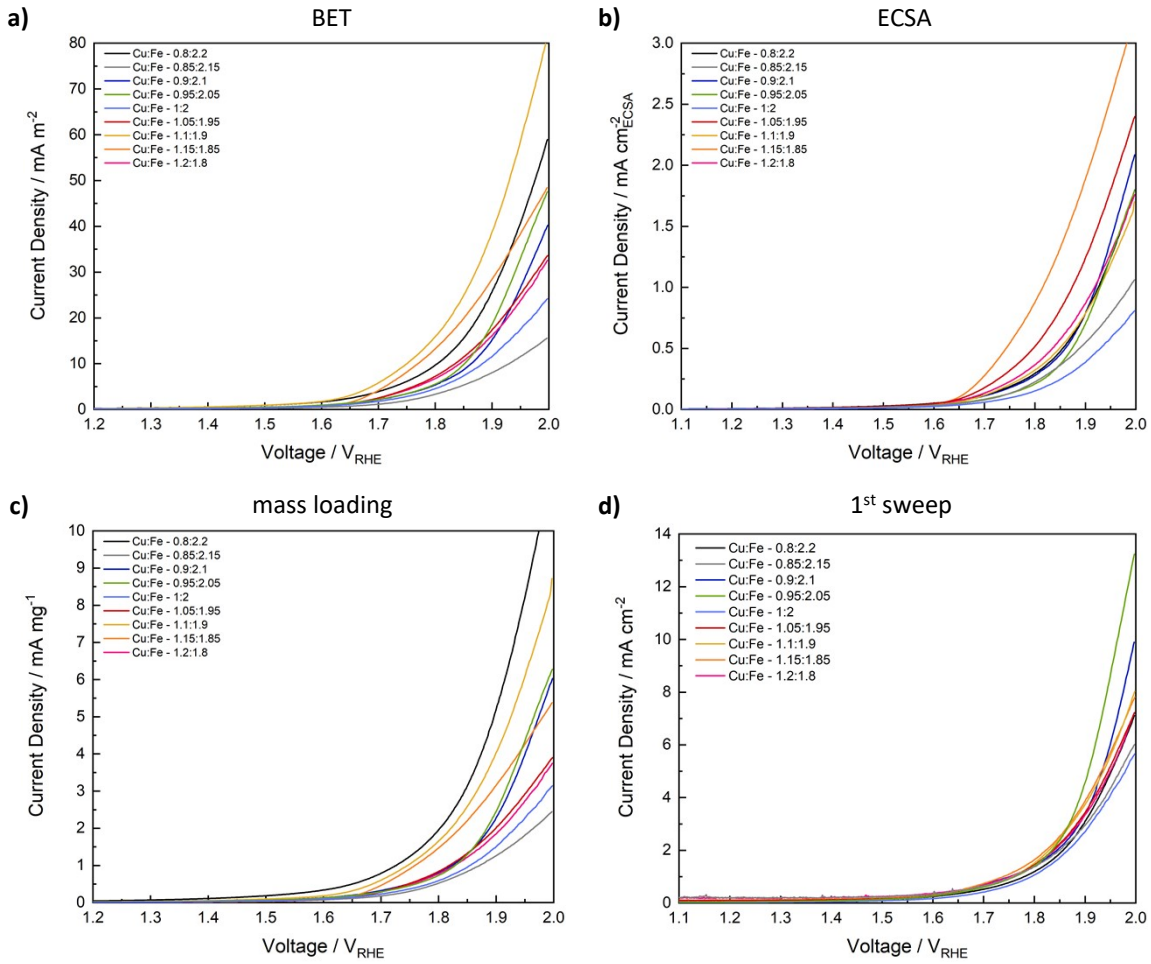

Figure S8 Final LSV corrected by the BET surface area (a), the ECSA determined after the LSVs (b), and the loaded mass (c). The first sweeps are shown in (d) for comparison.

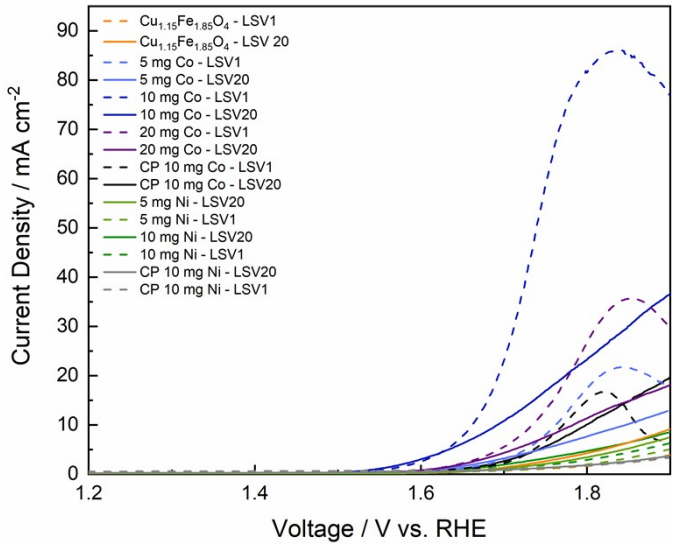

Figure S9 Linear sweep voltammetry to determine the activity of $Cu_{1.15}Fe_{1.85}O_4$ for the OER in the presence of low amounts of Co or Ni.

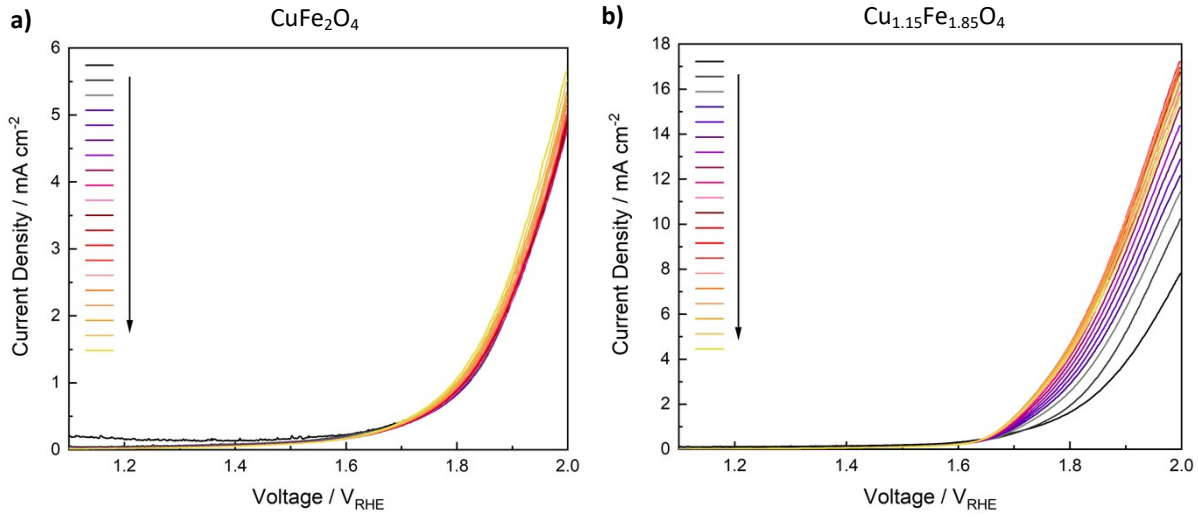

Figure S10 Current development with the number of anodic sweeps for both stoichiometric $CuFe_2O_4$ (a) and the most active composition of $Cu_{1.15}Fe_{1.85}O_4$ (b).

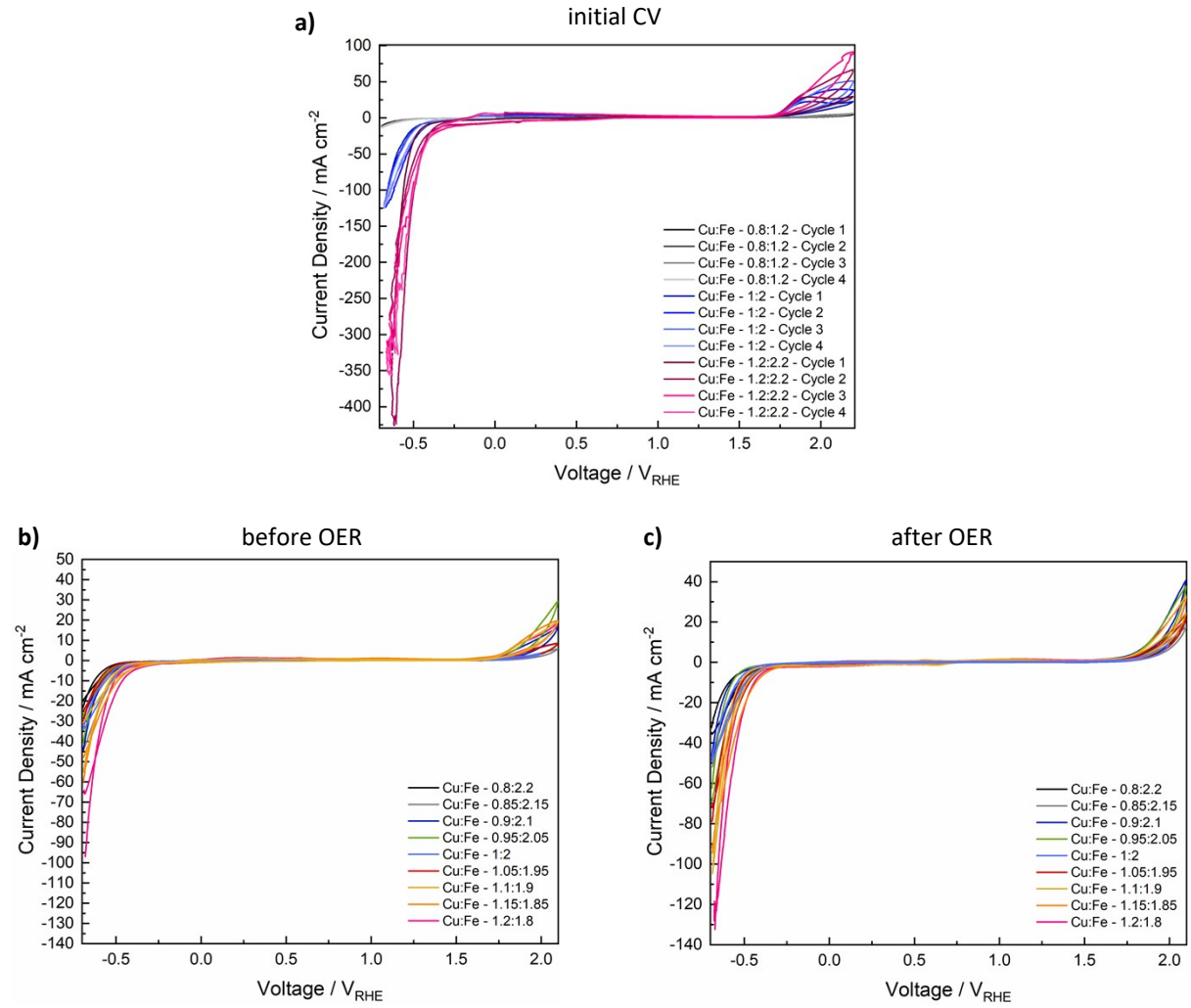

Figure S11 Changes in the initial CVs before the electrochemical measurements (in this case HER) are shown in (a). The third cycle for $CuFe_2O_4$ of different compositions are depicted in (b) before the OER and in (c) after.

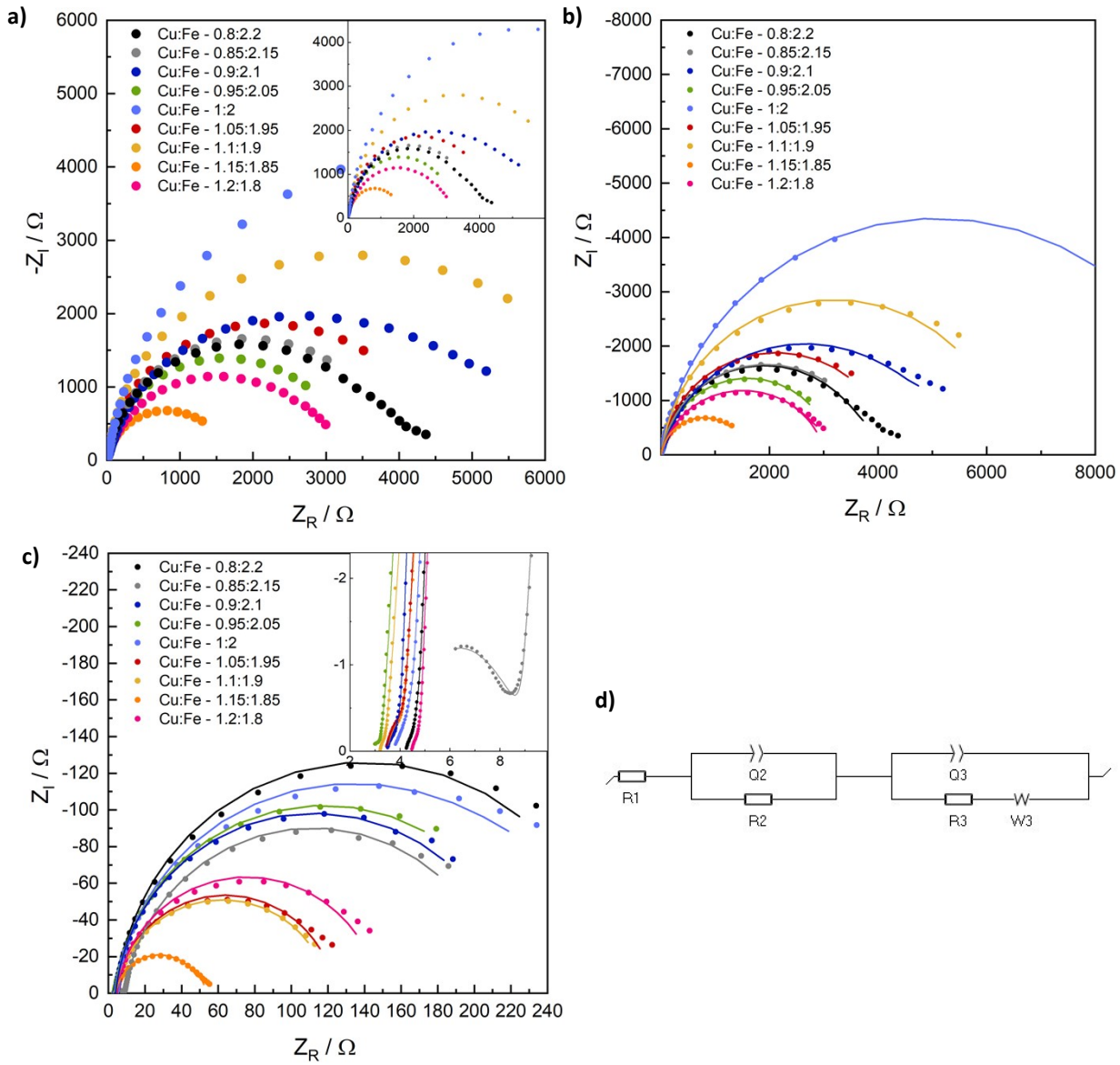

Figure S12 Nyquist plots at 1.7 V before the OER experiments (a), corresponding fits (b), and fitted Nyquist diagrams after the OER (c), together with the equivalent circuit used (d).

Table S4 Fit parameters for the Nyquist plots before and after the OER.

Cu/Fe	R1 / Ω	Q2 / F· s$^{(a-1)}$	R2 / Ω	Q3 / F· s$^{(a-1)}$	R3 / Ω	R1 / Ω	Q2 / F· s$^{(a-1)}$	R2 / Ω	Q3 / F· s$^{(a-1)}$	R3 / Ω
	Before OER					After OER				
0.36	4.007	0.0027	1.076	7.48E-6	3705	4.215	0.016	0.816	0.693	270
0.40	0.727	0.044	123.9	4.93E-5	3663	3.675	0.166	5.369	0.824	204.2
0.43	3.671	4.35E-4	16.36	0.851	5027	3.506	0.00269	0.568	7.88E-4	213.4
0.46	3.266	0.00153	24.65	4.81E-5	3153	2.837	0.363	3.606	0.00104	226.8
0.5	4.425	0.557	6.21	1.04E-5	9944	3.799	0.0032	0.876	0.574	238.4
0.54	3.794	0.00186	12.67	4.10E-5	4080	3.456	0.00117	0.823	7.99E-4	119.6
0.58	3.439	0.624	13.38	2.54E-5	6377	3.117	0.286	2.741	0.001	115.9
0.62	3.548	0.005	37.13	1.13E-4	1503	3.502	0.00113	0.726	0.849	47.21

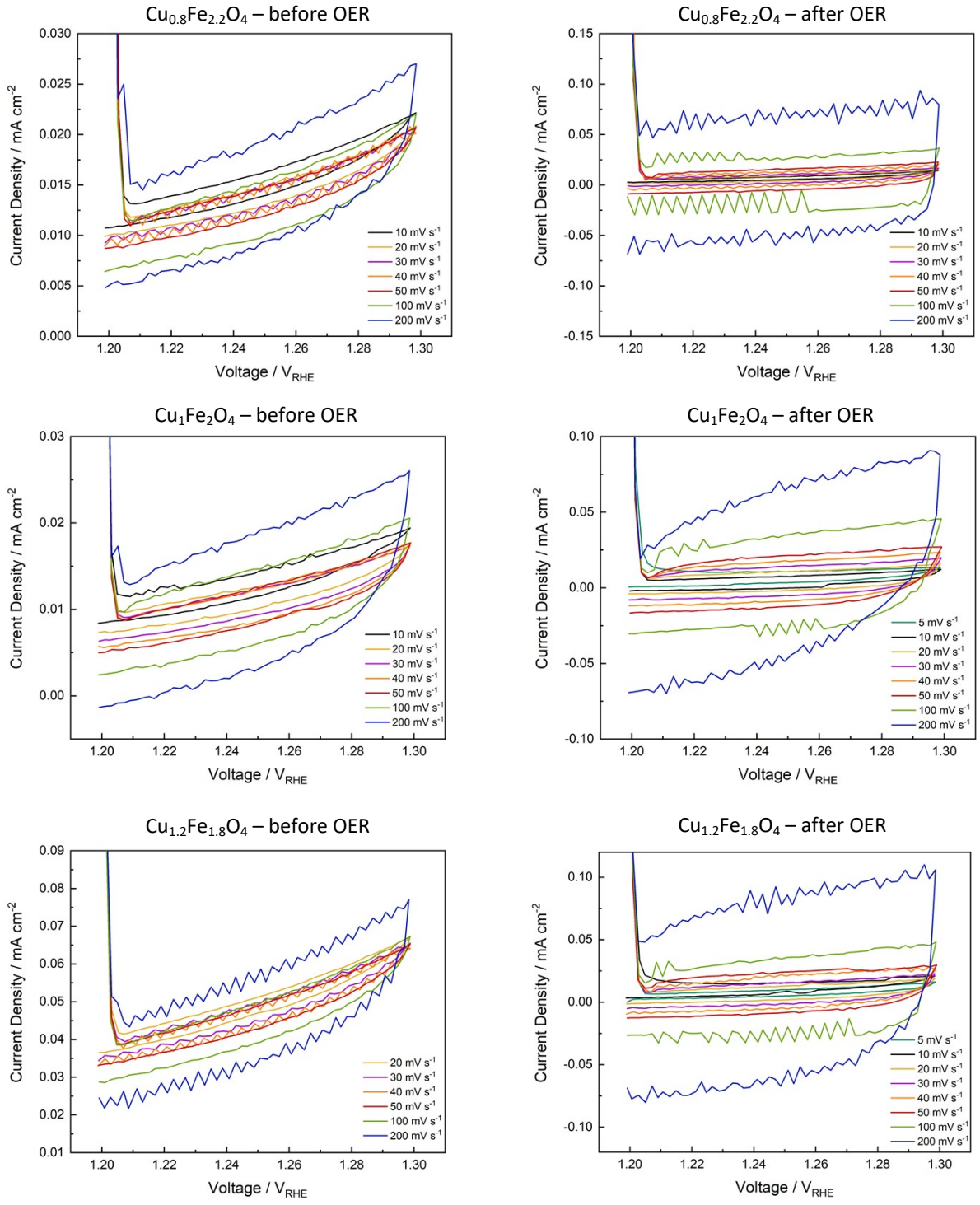

Figure S13 Cyclic voltammograms in a non-Faradaic region before and after the OER at different scan rates, to determine the double layer capacitance for $CuFe_2O_4$ with a low Cu-content ($Cu_{0.8}Fe_{2.2}O_4$ –(a) and (b)), stoichiometric $CuFe_2O_4$ (c) and (d), and with a high Cu-content ($Cu_{1.2}Fe_{1.8}O_4$ - (e) and (f).

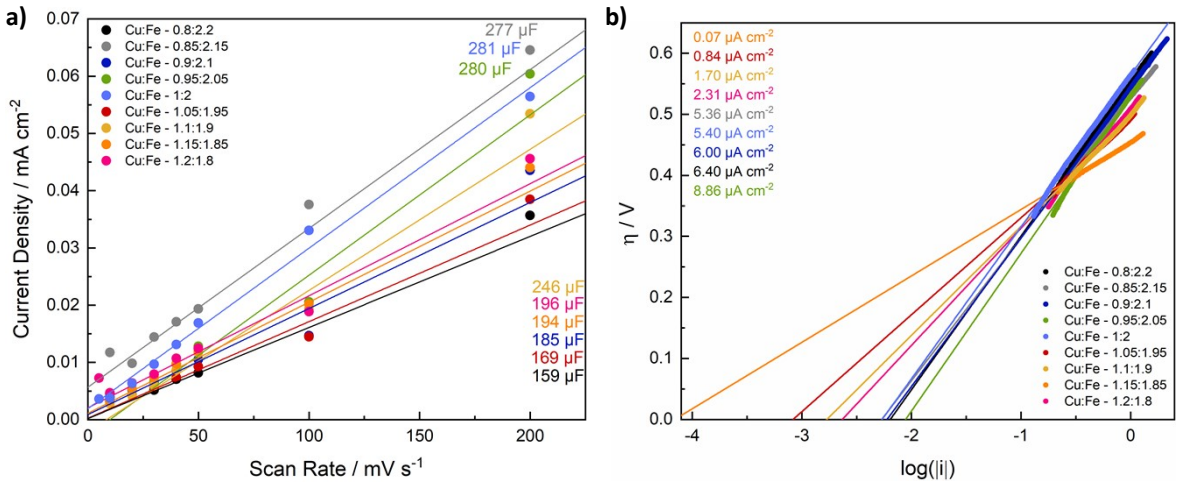

Figure S14 C_{DL} determined from the average of anodic and cathodic charging currents after the OER experiments (a) and exchange current densities extrapolated from the Tafel plots (b).

Table S5 ECSA determined before and after the OER and HER, respectively, for $CuFe_2O_4$ of varied composition.

Cu:Fe- Ratio	ECSA - before OER	ECSA – after OER	ECSA – before HER	ECSA – after HER
0.8:2.2	0.6 cm^2	4.0 cm^2	15 cm^2	180 cm^2
0.85:2.15	4.8 cm^2	6.9 cm^2	39 cm^2	315 cm^2
0.9:2.1	1.8 cm^2	4.6 cm^2	24 cm^2	66 cm^2
0.95:2.05	3.2 cm^2	7.0 cm^2	35 cm^2	173 cm^2
1:2	1.0 cm^2	7.0 cm^2	74 cm^2	224 cm^2
1.05:1.95	3.9 cm^2	4.2 cm^2	231 cm^2	151 cm^2
1.1:1.9	3.2 cm^2	6.2 cm^2	161 cm^2	450 cm^2
1.15:1.855	5.3 cm^2	4.9 cm^2	196 cm^2	162 cm^2
1.2:1.8	1.4 cm^2	4.9 cm^2	178 cm^2	610 cm^2

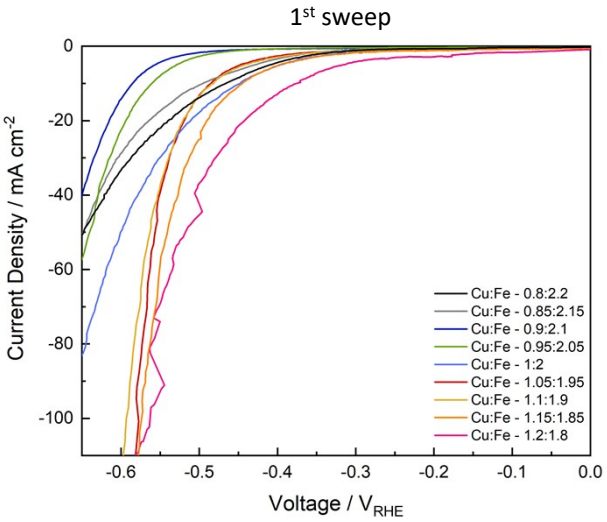

Figure S15 Initial LSV curve before the HER for $CuFe_2O_4$ of varied composition.

Figure S16 Development of the current density with the number of LSV scans for a stoichiometric $CuFe_2O_4$ (a)

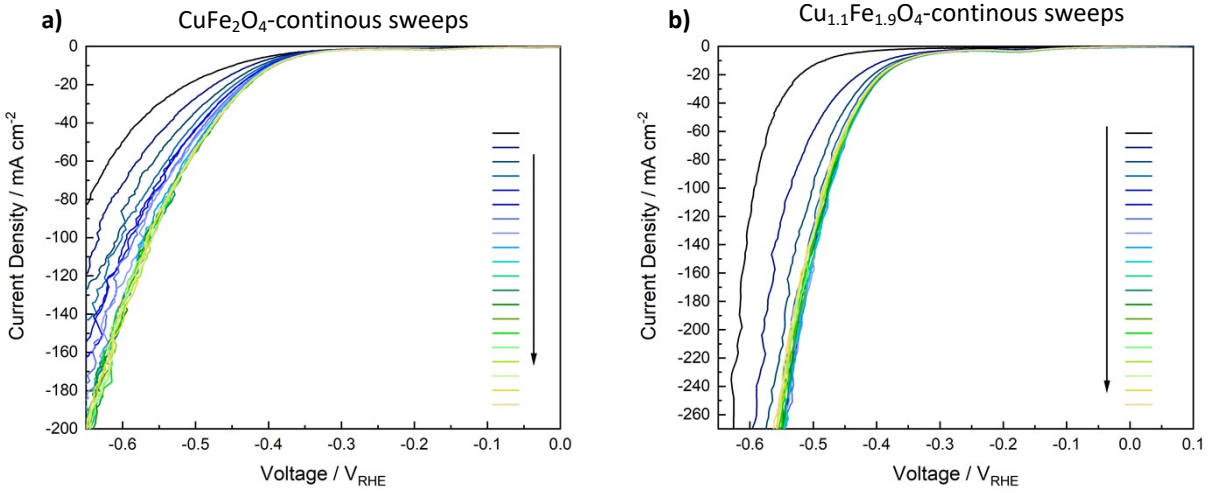

and the most active composition $Cu_{1.1}Fe_{1.9}O_4$ (b).

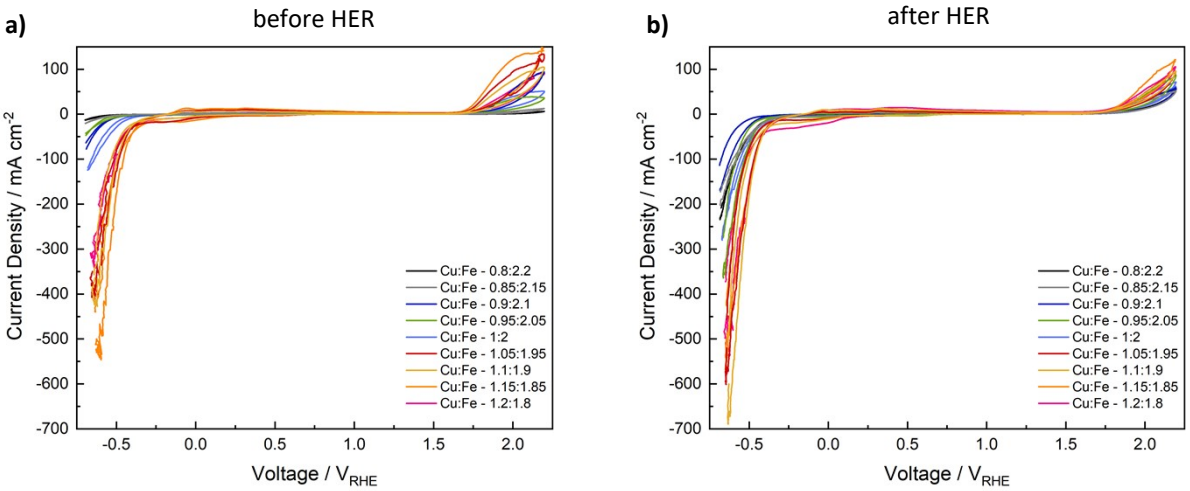

Figure S17 Cyclic voltammograms 3rd cycle) before (a) and after (b) the HER for $CuFe_2O_4$ of varied composition.

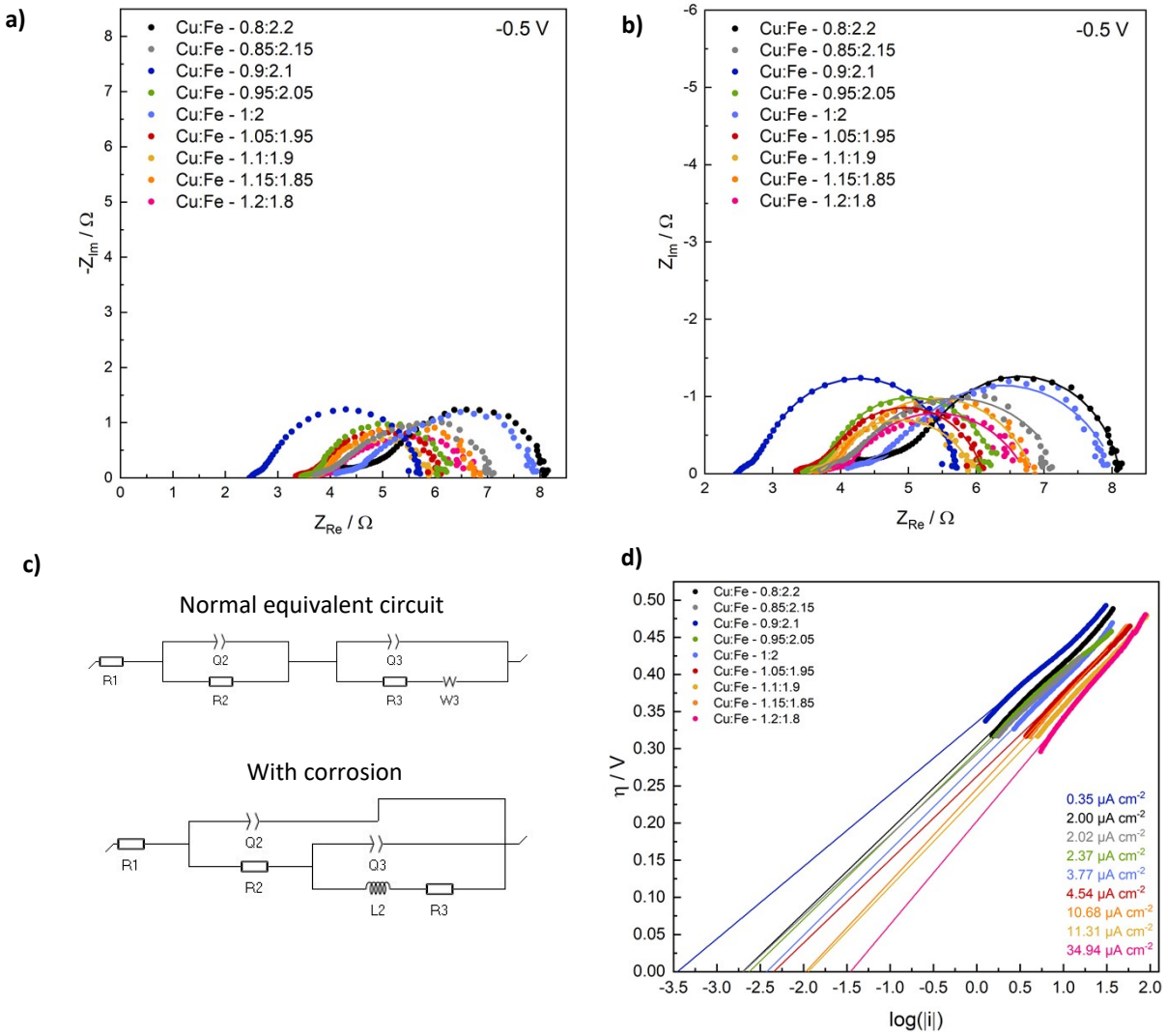

Figure S18 Nyquist plots after the HER at -0.5 V (a), corresponding fits (b), and equivalent circuits used for the plots after the HER, as well as potential equivalent circuits taking into account corrosion phenomena/ adsorbed species (c), and exchange current densities derived from Tafel plots (d).

Table S6 Fit parameters for the Nyquist plots after the HER.

Cu/Fe	R1 / Ω	Q2 / F· s$^{(a-1)}$	R2 / Ω	Q3 / F· s$^{(a-1)}$	R3 / Ω	Q4 / F· s$^{(a-1)}$	R4 / Ω
0.36	2.156	0.014	0.952	0.00382	2.522	0.00341	2.528
0.40	3.748	0.00153	0.385	0.00885	3.144		
0.43	2.463	0.00298	2.759	0.017	0.493		
0.46	3.447	0.00757	0.356	0.00745	2.507		
0.5	4.008	1.18E+19	0.335	0.03	1.18	0.00695	2.903
0.54	3.341	0.023	0.69	0.00619	2.082		
0.58	3.529	0.0025	0.241	0.012	2.218		
0.62	3.654	0.017	0.402	0.00701	2.781		

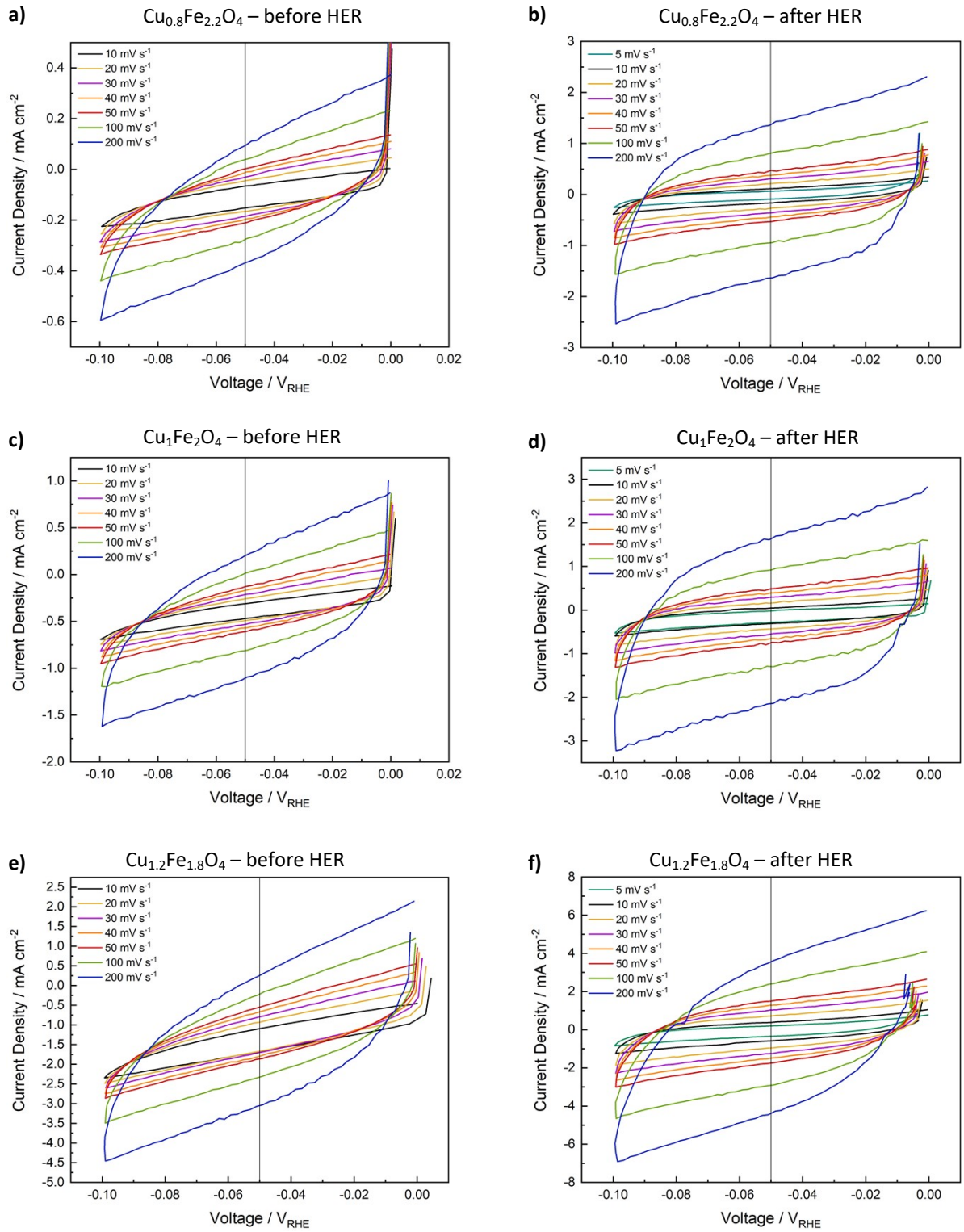

Figure S19 Cyclic voltammograms before and after the HER, to determine double layer capacitance for with a low Cu-content ($Cu_{0.8}Fe_{2.2}O_4$ –(a) and (b)), stoichiometric $CuFe_2O_4$ (c) and (d), and with a high Cu-content ($Cu_{1.2}Fe_{1.8}O_4$ - (e) and (f).

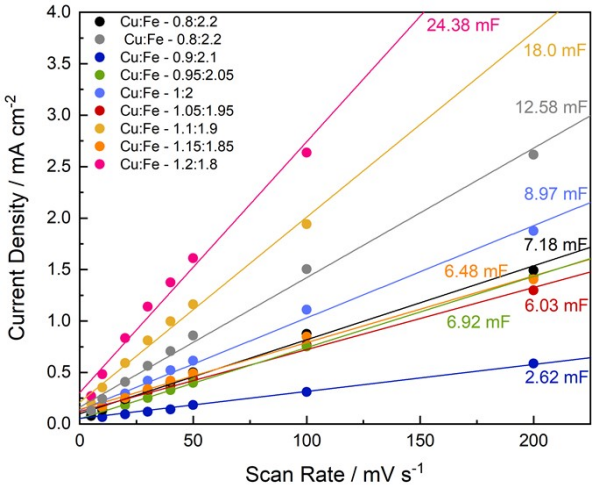

Figure S20 Double layer capacitance determined from the average of anodic and cathodic charging current after the HER.

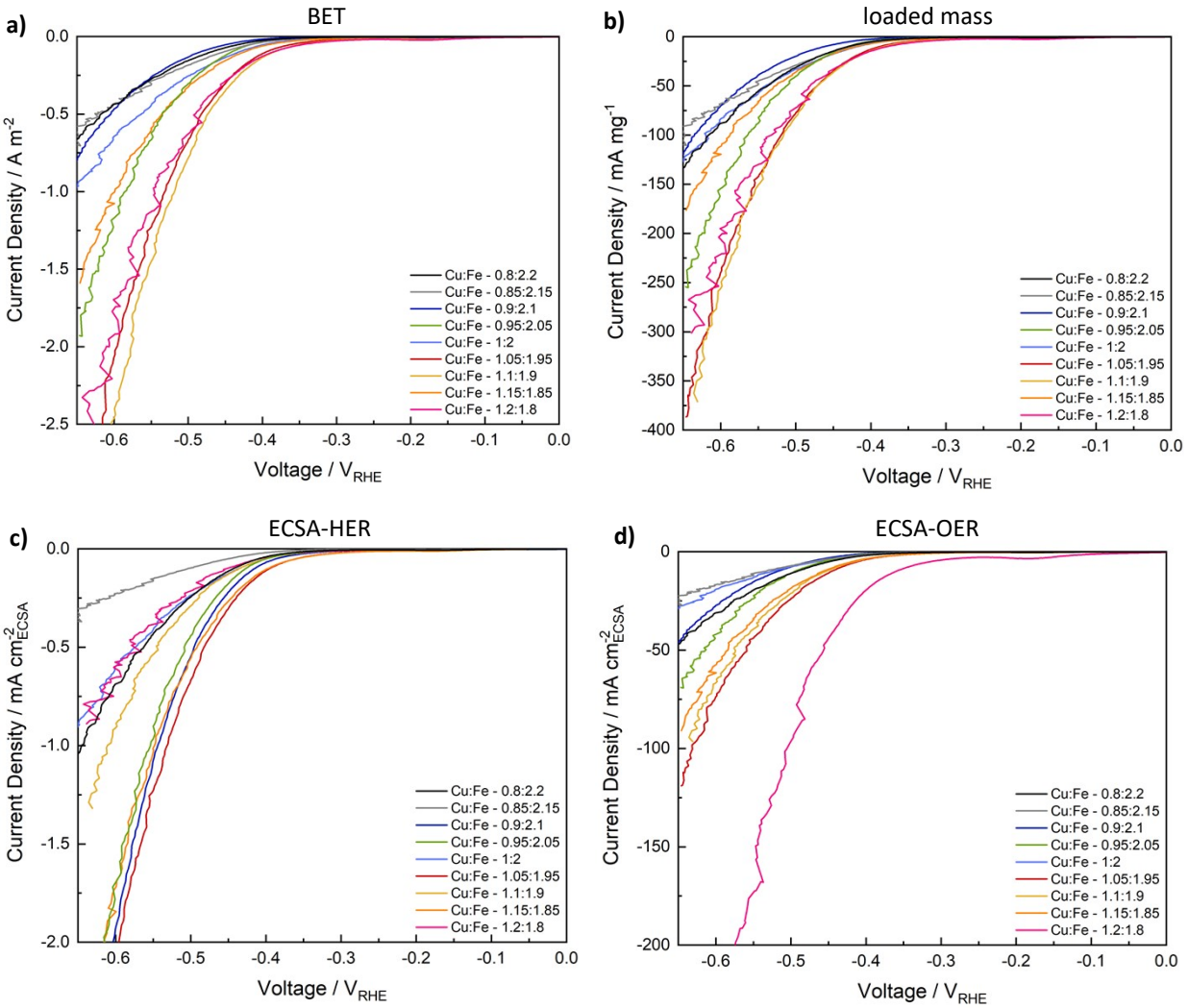

Figure S21 Final LSV curves normalised to the BET surface area (a), the loaded mass (b), the ECSA determined after the HER (c) and the ECSA determined between 1.2 and 1.3 V after the OER.

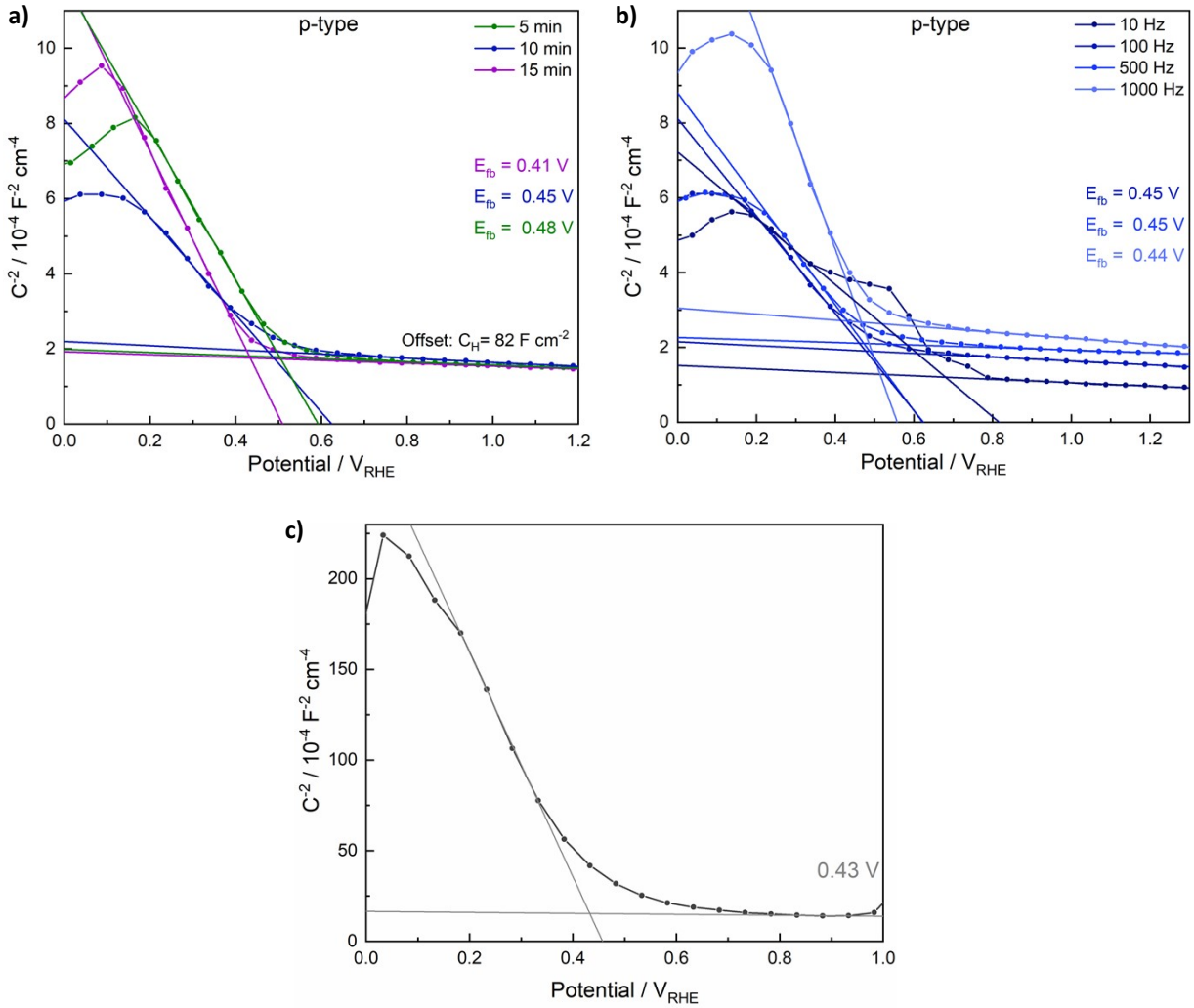

Figure S22 Mott-Schottky plots at 100 Hz for $CuFe_2O_4$ electrodes (stoichiometric) prepared via electrophoretic deposition for different times at 15 V (a) and for the electrode with a deposition time of 10 min at various frequencies (b). An additional measurement at 1000 Hz in 1 M KOH was performed in order to validate the pH dependence of the flat band potential (c).

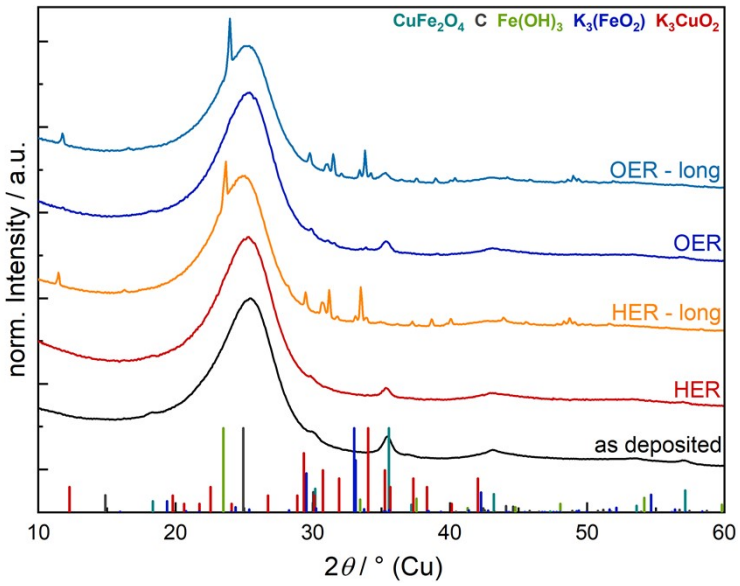

Figure S23 XRD patterns of electrodes before and after the HER and OER, respectively. Following ICDD reference cards were used for the identification: 01-077-0010 – $CuFe_2O_4$; 01-074-2329 – C (graphite); 00-046-1436 – $Fe(OH)_3$; 00-038-0971 – K_3CuO_2; 01-081-1805 – $K_3(FeO_2)$.

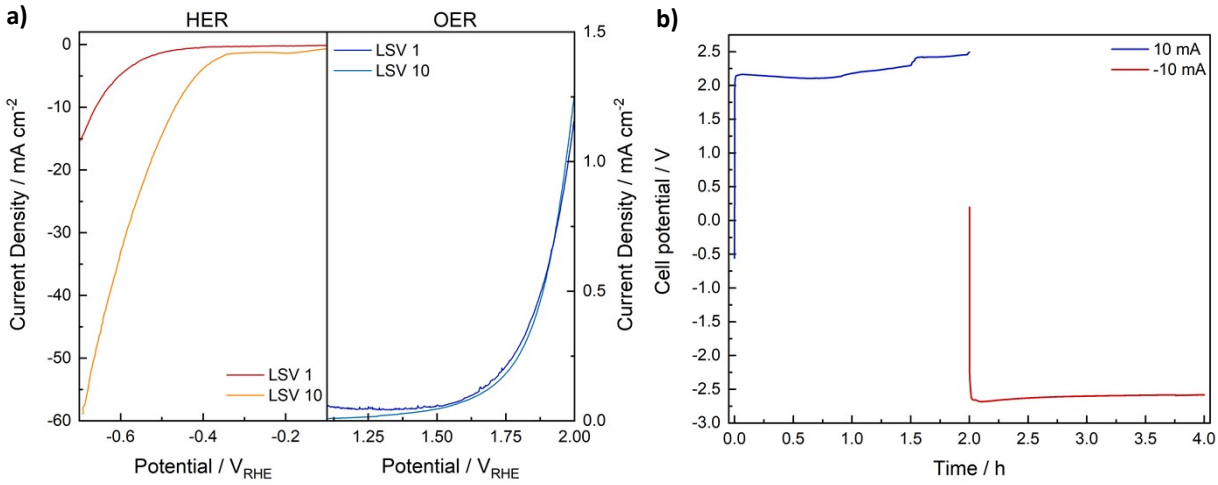

Figure S24 LSV scans for both HER and OER in a three-electrode setup with the counter electrode being similarly made by drop-casting stoichiometric $CuFe_2O_4$ onto carbon paper (a), and subsequent cell potential measured for first 10 mA and then -10 mA at the working electrode in the same setup (b).

Table S7 Overpotentials for the ORR with $CuFe_2O_4$ with different Cu/Fe-ratios.

Cu:Fe-Ratio	η_{ORR} – 10 mA cm^{-2}	η_{ORR} – 5 mA cm^{-2}
0.8:2.2	767 mV	639 mV
0.85:2.15	656 mV	577 mV
0.9:2.1	762 mV	643 mV
0.95:2.05	722 mV	617 mV
1:2	720 mV	631 mV
1.05:1.95	708 mV	608 mV
1.1:1.9	765 mV	646 mV
1.15:1.855	726 mV	614 mV
1.2:1.8	714 mV	611 mV

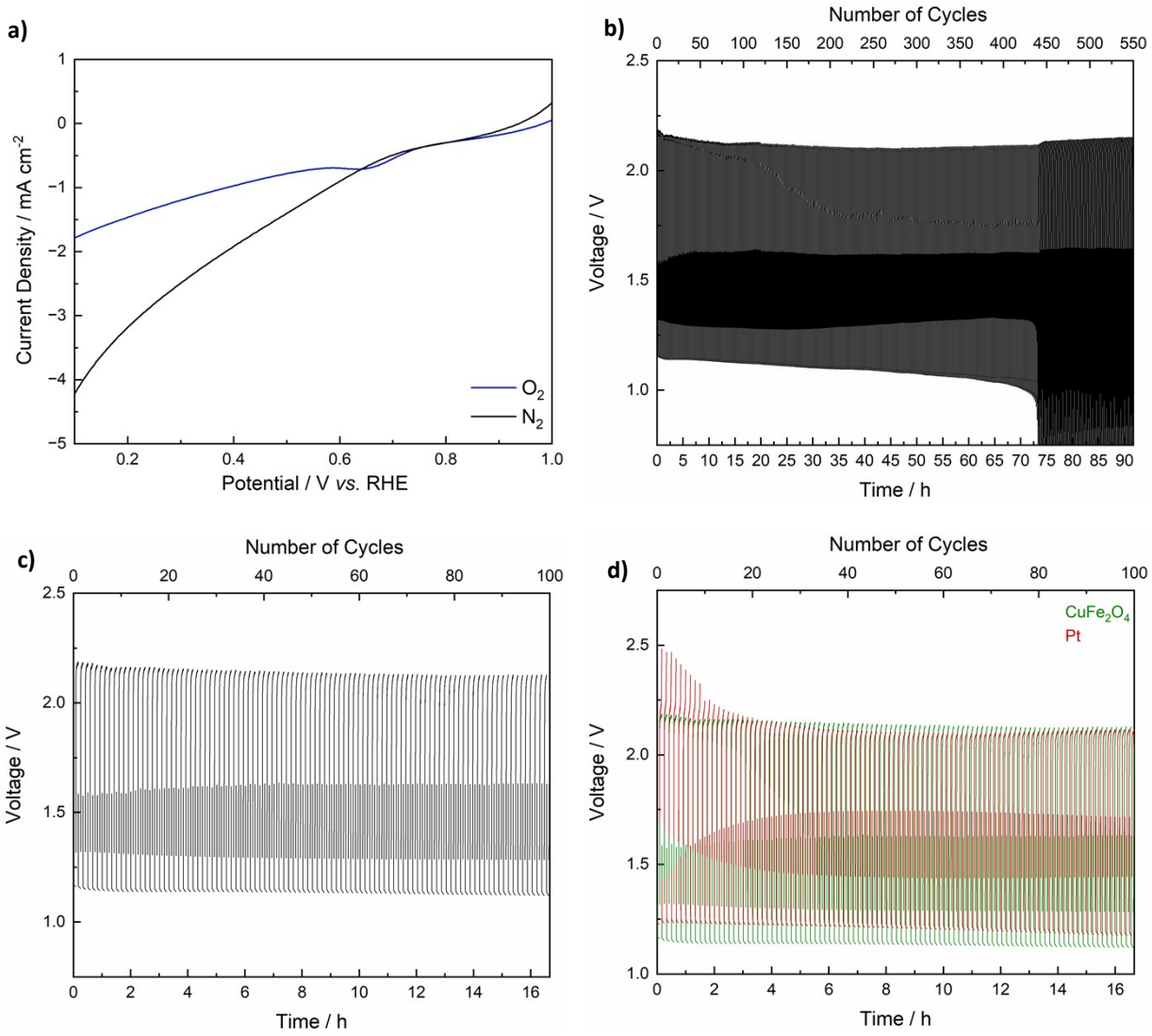

Figure S25 The 10th consecutive LSV scan for the bare GDL in O_2 and N_2 is shown in (a). Repeated charge/ discharge cycles (5 min each) for a $CuFe_2O_4$ GDE in the Zn-air battery (50 mA cm^{-2}) over 550 cycles (b), and an excerpt of the first 100 cycles (c). The comparison with the commercial Pt/C-GDE is depicted in (d).

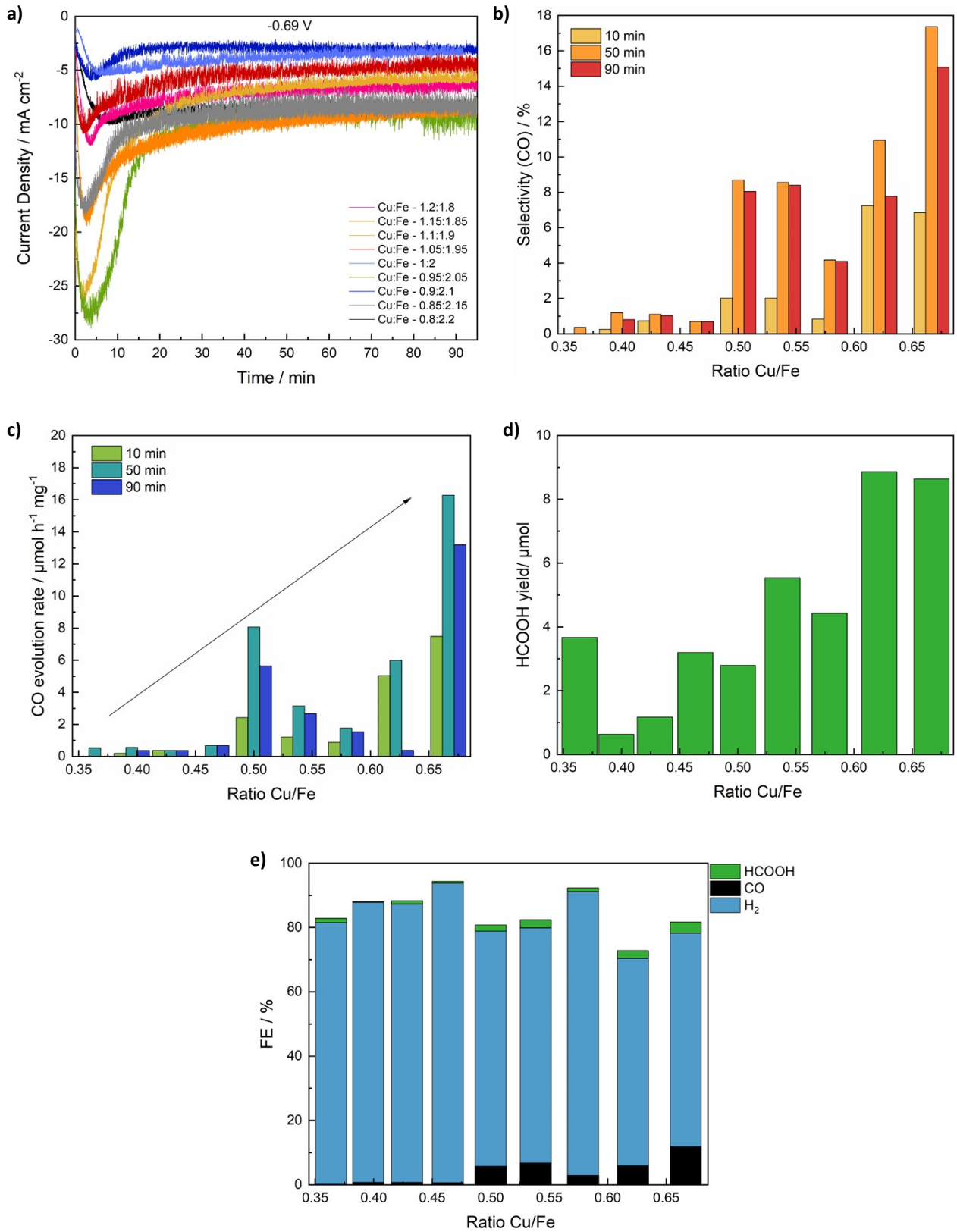

Figure S26 Current densities measured for the CO_2RR with $CuFe_2O_4$ of different composition at a potential of -0.69 V vs. RHE (a), calculated selectivity for CO based on the detected gaseous products (b), CO yields normalised to mass loading (c), measured amounts of HCOOH (d) and sum of the Faradaic efficiencies (e).

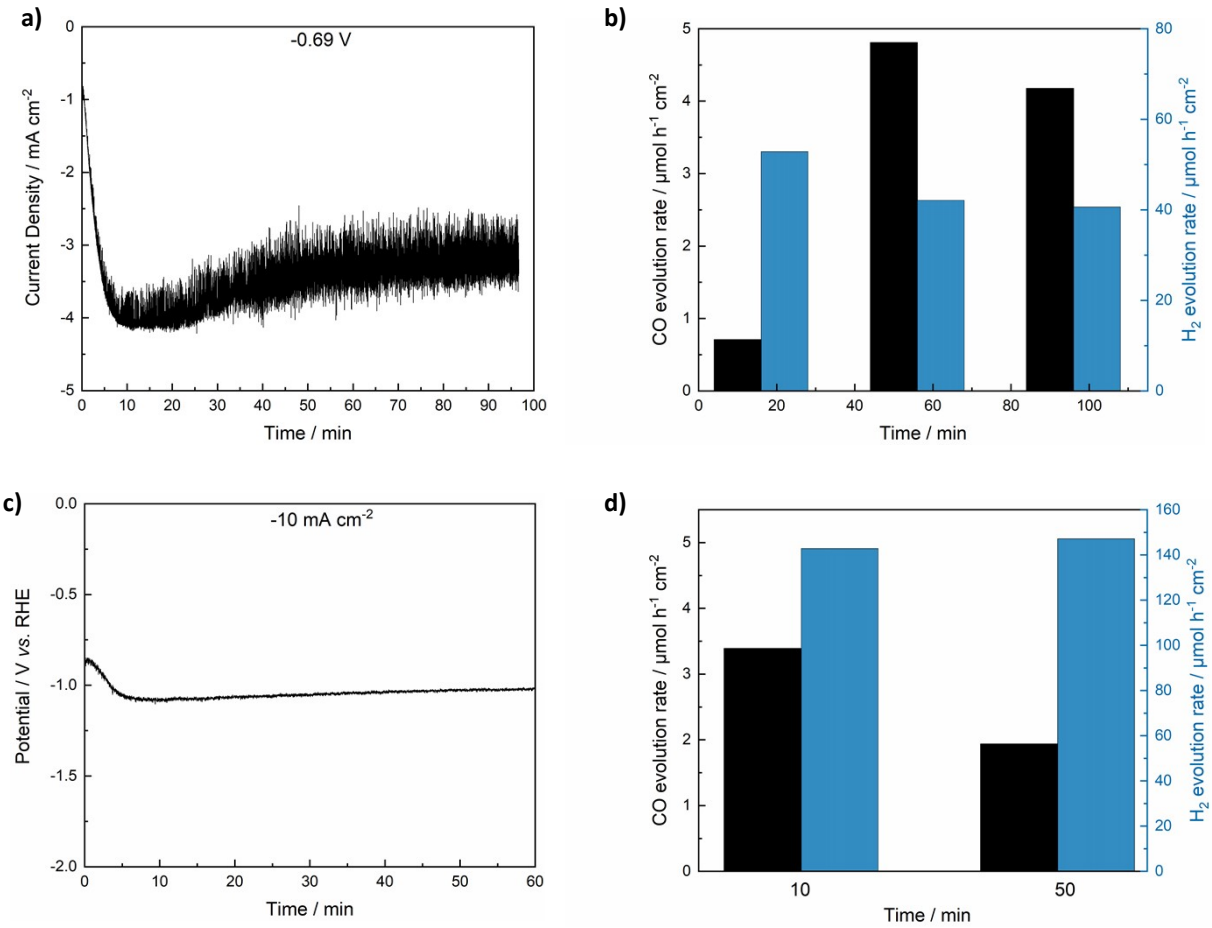

Figure S27 Current densities measured for $CuFe_2O_4$ during chronoamperometry at -0.69 V for the electrochemical CO_2RR, with a second $CuFe_2O_4$ electrode used as counter electrode (a). The corresponding CO and H_2 yields are shown in (b). Subsequently, the working electrode potential was monitored at 10 mA cm^{-2} (c), and the corresponding CO and H_2 yields are depicted in (d).

Table 8 Activity comparison with related electrocatalysts.

	Material	Overpotential	Products	Electrolyte & Substrate	Synthesis	Reference
HER	Cu-Fe_3O_4	222 mV (50 mA cm^{-2})		1 M KOH, Fe-foam	Hydrothermal	[3]
	Fe_3O_4	315 mV (50 mA cm^{-2})		1 M KOH, Fe-foam	Hydrothermal	[3]
	Fe_2O_3-NC	245-438 mV (10 mA cm^{-2})		1 M KOH, GC	Calcination of nitrates with $C_2H_4N_4$	[4]
	Fe_2O_3	312-423 mV (10 mA cm^{-2})		0.1 M KOH, GC	Hydrothermal	[5]
	Fe_2O_3	302 mV (10 mA cm^{-2})		1 M KOH, Fe-foam	CVD	[6]
	Cu foam	372 mV (10 mA cm^{-2})		1 M KOH		[7]
	Cu	320 – 740 mV (5 mA cm^{-2})		0.1 M KOH		[8]
	This work	**342 mV (10 mA cm^{-2})**		**1 M KOH, CP**	**Microwave**	
OER	$CuFe_2O_4$	369 mV (10 mA cm^{-2})		1 M KOH, Ni-foam	Sol-gel synthesis + ball milling	[9]
	$CuFe_2O_4$ fibres	367 mV (10 mA cm^{-2})		1 M KOH, Ni-foam	Solution blow spinning	[10]
	$CuFe_2O_4$@porous carbon nanowires	359 mV (10 mA cm^{-2})		1 M KOH, self supported	Electrospinning	[11]
	$CuFe_2O_4$	474 mV (10 mA cm^{-2})		1 M KOH RDE (GC)	Calcination of acetate precursors	[11]
	Fe_2O_3	551 mV (10 mA cm^{-2})		1 M KOH RDE (GC)	Calcination of acetate precursors	[11]
	FeOOH	853 mV (10 mA cm^{-2})		1 M KOH, Ti	Hydrothermal	[12]
	Fe_3O_4	415 mV (10 mA cm^{-2})		1 M KOH, Ti	Hydrothermal + annealing in Ar/H_2	[12]
	CuO	475 mV (10 mA cm^{-2})		1 M KOH, GC/ FTO	In-situ from a Cu(II)-ethylenediamine compolex	[13]
	CuO/Ni	364 mV (10 mA cm^{-2})		1 M KOH, Ni foam	electrodeposition	
	CuO	420 mV (10 mA cm^{-2})		1 M KOH, GC	Molten salt	[14]
	This work	**684 mV (10 mA cm^{-2})**		**1 M KOH, CP**	**Microwave**	
ORR	Cu-$CuFe_2O_4$/C	Onset: 884 mV*		0.1 M KOH, RDE, 1600 rpm	Solvothermal	[15]
	Fe_2O_3	Onset: -890 mV vs Ag/Ag Cl*		0.1 M KOH, RDE, 1600 rpm	Solvothermal	[15]
	γ-Fe_2O_3/δ-FeOOH	Onset 730 mV		0.5 M KOH, RDE	Non-stationary electrolysis	[16]
	Fe_3O_4/Fe/C	Onset: ~824 mV*		6 M KOH, GDE on Ni	Microwave sintering	[17]

This work	**Onset: ~800 mV**		**4 M KOH, GDE**	**Microwave**

*Assuming a pH of 14

References

[1] M. C. Biesinger, *Surf. Interface Anal.* **2017**, *49*, 1325–1334.

[2] M. C. Biesinger, B. P. Payne, A. P. Grosvenor, L. W. M. Lau, A. R. Gerson, R. S. C. Smart, *Appl. Surf. Sci.* **2011**, *257*, 2717–2730.

[3] C. Yang, W. Zhong, K. Shen, Q. Zhang, R. Zhao, H. Xiang, J. Wu, X. Li, N. Yang, *Adv. Energy Mater.* **2022**, *12*, DOI 10.1002/aenm.202200077.

[4] J. Jiang, L. Zhu, Y. Sun, Y. Chen, H. Chen, S. Han, H. Lin, *J. Power Sources* **2019**, *426*, 74–83.

[5] R. N. Ali, H. Naz, X. Zhu, J. Xiang, G. Hu, B. Xiang, *Mater. Res. Express* **2018**, *6*, DOI 10.1088/2053-1591/aaf0dd.

[6] Q. Hao, L. Zhang, Y. Gao, D. Cao, J. Zhao, Y. Li, C. Liu, Z. Qiao, W. He, H. Liu, *ACS Appl. Energy Mater.* **2022**, *5*, 1793–1800.

[7] X. Hu, X. Tian, Y. W. Lin, Z. Wang, *RSC Adv.* **2019**, *9*, 31563–31571.

[8] P. Farinazzo Bergamo Dias Martins, P. Papa Lopes, E. A. Ticianelli, V. R. Stamenkovic, N. M. Markovic, D. Strmcnik, *Electrochem. commun.* **2019**, *100*, 30–33.

[9] L. S. Ferreira, T. R. Silva, V. D. Silva, R. A. Raimundo, T. A. Simões, F. J. A. Loureiro, D. P. Fagg, M. A. Morales, D. A. Macedo, *Adv. Powder Technol.* **2022**, *33*, 103391.

[10] V. D. Silva, L. S. Ferreira, T. A. Simões, E. S. Medeiros, D. A. Macedo, *J. Colloid Interface Sci.* **2019**, *540*, 59–65.

[11] M. Li, M. Lu, J. Yang, J. Xiao, L. Han, Y. Zhang, X. Bo, *J. Alloys Compd.* **2019**, *809*, 151766.

[12] L. Gao, C. Tang, J. Liu, L. He, H. Wang, Z. Ke, W. Li, C. Jiang, D. He, L. Cheng, et al., *Energy Environ. Mater.* **2021**, *4*, 392–398.

[13] X. Liu, S. Cui, M. Qian, Z. Sun, P. Du, *Chem. Commun.* **2016**, *52*, 5546–5549.

[14] M. Qian, X. Liu, S. Cui, H. Jia, P. Du, *Electrochim. Acta* **2018**, *263*, 318–327.

[15] B. J. Borah, Y. Yamada, P. Bharali, *ACS Appl. Energy Mater.* **2020**, *3*, 3488–3496.

[16] T. Molodtsova, M. Gorshenkov, S. Kubrin, A. Saraev, A. Ulyankina, N. Smirnova, *J. Taiwan Inst. Chem. Eng.* **2022**, *140*, 104569.

[17] Z. Zhang, D. Zhou, J. Liao, X. Bao, S. Luo, *J. Alloys Compd.* **2019**, *786*, 134–138.